Observing floe-scale sea ice motion in the Greenland Sea marginal ice zone during summer

Journal:	*Annals of Glaciology*
Manuscript ID	Draft
Manuscript Type:	Article
Date Submitted by the Author:	n/a
Complete List of Authors:	Watkins, Daniel; Brown University, Center for Fluid Mechanics Buckley, Ellen; Brown University, Center for Fluid Mechanics Kim, Minki; Brown University, Center for Fluid Mechanics Martinez Wilhelmus, Monica; Brown University, Center for Fluid Mechanics
Keywords:	Sea ice, Sea-ice dynamics, Ice/ocean interactions
Abstract:	The Fram Strait is a key region for ice export, linking the Arctic with the world ocean. We present floe-scale observations of sea ice motion in the Fram Strait marginal ice zone (MIZ) derived from moderate-scale optical imagery spanning the 2003-2020 period. Tracked ice floes provide Lagrangian measures of ice motion during the spring and summer. We show that the floe size distribution affects the rotation rates and fluctuating velocities of sea ice floes. Using simulations using a quasi-geostrophic ocean model and a discrete element model, we show that ocean eddy forcing alone can produce the distinct non-Gaussian velocity anomaly distributions seen in observations. The scale of the velocity distributions decreases with increasing floe size and with increasing distance from the ice edge. Similarly, we show that the rotation rate distribution in both observations and simulations narrows with increasing floe size. Finally, we show that the deformation rates measured from tracked MIZ ice floes reproduce the power law scaling seen in the central Arctic, with the deformation rate decreasing as the scale of observations increases. The observations presented here provide a new avenue for sea ice model development and validation in the summer MIZ.

Observing floe-scale sea ice motion in the Greenland Sea marginal ice zone during summer

Daniel M. WATKINS,[1] Ellen M. BUCKLEY,[1] Minki KIM,[1] Monica M. WILHELMUS[1]

[1]*Center for Fluid Mechanics, Brown University, Providence, RI, USA*

Correspondence: Monica M. Wilhelmus <mmwilhelmus@brown.edu>

ABSTRACT. Sea ice dynamics in the marginal ice zone are complex, resulting from coupled motions of the atmosphere and ocean interacting with a heterogeneous sea ice surface. The distribution of sea ice floe shapes and sizes affects the spatial coherence of ice motion and the response of ice to stresses. The Fram Strait is a key region for ice export, linking the Arctic with the world ocean. Complex currents, strong deformation, and low spatial correlation result in high uncertainty in sea ice drift observations. We present floe-scale observations of sea ice motion in the Fram Strait marginal ice zone (MIZ) derived from moderate-scale optical imagery spanning the 2003-2020 period. Tracked ice floes provide Lagrangian measures of ice motion during the spring and summer. We show that the floe size distribution affects the rotation rates and fluctuating velocities of sea ice floes. Simulations using a quasi-geostrophic ocean model and a discrete element model show that ocean eddy forcing alone can produce the distinct non-Gaussian velocity anomaly distributions seen in observations. The scale of the velocity distributions decreases with increasing floe size and with increasing distance from the ice edge. Similarly, we show that the rotation rate distribution in both observations and simulations narrows with increasing floe size. Finally, we show that the deformation rates measured from tracked MIZ ice floes reproduce the power law scaling seen in the central Arctic, with the deformation rate decreasing as the scale of observations increases. The observations presented here provide a new avenue for sea ice model development and validation in the summer MIZ.

INTRODUCTION

Sea ice dynamics occur across a continuum of time and space scales (McNutt and Overland, 2003), while sea ice observation systems are constrained by their minimum spatial resolution and reporting frequency (Lee and others, 2022). Advances in computational capability enable modeling centers to run Earth system models on ever-finer spatial grids. Traditional models of sea ice motion rely on a continuum approximation of sea ice dynamics (e.g., Hibler (1979)). Such models successfully reproduce many aspects of sea ice dynamics and thermodynamics (Hutter and others, 2018; Zhang, 2021). However, in the marginal ice zone (MIZ), and in other regions with high sub-grid variability, alternative approaches are needed (Herman, 2022). Validation and development of models capable of simulating small-scale sea ice variability requires observations of multi-scale sea ice motion, including observations of motion at the floe scale.

Sea ice motion in the Fram Strait and Greenland Sea is highly variable, and uncertainty in drift observations is high (e.g., Sumata and others (2014)). Ice motion results from a complex balance of forces, including atmospheric, oceanic, and internal ice stresses, Coriolis acceleration, surface tilt, and surface waves (Dumont, 2022; Dai and others, 2019; Hibler, 1979). Atmospheric and oceanic forcing are tightly coupled to the evolving sea ice interface. The effect of sharp contrasts in boundary conditions between ice-covered and open seas at the sea ice edge results in the formation of atmospheric jets (Guest and others, 2018), affecting ice motion (Heorton and others, 2014). Ocean currents (including tides) respond to seafloor topography, which can imprint on sea ice dynamics (Hakkinen, 1987; Watkins and others, 2023).

The imprint of ocean eddies on sea ice can be seen with in situ measurements (Timmermans and others, 2008) and remote sensing imagery (Manley, 1987; Johannessen and others, 1987; Kozlov and Atadzhanova, 2021). Near-surface eddies have been observed throughout the Arctic Ocean (Kozlov and others, 2019); eddy kinetic energy is particularly high in the Greenland Shelf and Fram Strait region (Von Appen and others, 2022; Armitage and others, 2017). The presence of a rich eddy field imparts a vorticity signal into ice floe motion, inducing rotation of ice floes (Manucharyan and others, 2022)and producing deformation (Zhang and others, 1999).

Spatial variability in ice motion is directly related to the floe size and the geometry of floe-floe interactions, which can lead to multifloe and aggregate motions (McNutt and Overland, 2003). The size of ice floes in the MIZ displays fractal-like power-law scaling, with bounds on minimum and maximum floe sizes determined by wave properties and coastal geometry. Floes become larger due to pieces of ice interlocking, rafting, ridging and fusing, or decrease in size due to fracture (such as through collision with other floes, wave interaction, or interaction with coastal features) and melt.

The floe size distribution (FSD) is a probability distribution characterizing the likelihood of finding ice floes of a given size in a region. The FSD affects the melt rate of ice, the spatial correlation of the sea ice response to atmospheric and oceanic stresses, and the partitioning of solar heat into the upper ocean. Rothrock and Thorndike (1984) introduced the idea of fitting a power law to the FSD such that the probability $p(x)$ of a floe with area x is given by

$$p(x) = cx^{-\alpha} \tag{1}$$

where c is a normalization constant. The parameter α is the slope of the power law distribution. Numerous physical reasons cause FSD slopes to vary, including the seasonal cycle, storms and wave events, and geographic differences (Inoue, 2004; Perovich and Jones, 2014; Geise and others, 2017; Hwang and others, 2017). Not all FSDs can be described with Equation 1, as acknowledged by Rothrock and Thorndike (1984), and statistical issues can lead to varying α estimates (Clauset and others, 2009). Nevertheless, power laws have been frequently applied in the literature, producing a wide range of estimates for the α parameter (c.f. Stern and others (2018b) comparing studies from 1984-2018).

Ice deformation, too, shows fractal-like properties across moderate to large scales, including scale invariance in space and time (Marsan and others, 2004; Martin and Thorndike, 1985; Thorndike, 1986; Rampal and others, 2008, 2019). Properties of the exponential relationships between deformation and the time and space scales of measurements vary regionally and seasonally (Kwok, 2006; Stern and Lindsay, 2009; Oikkonen and others, 2017). Spectral characteristics of sea ice deformation transition from red noise to increasingly white noise as averaging length scales decrease (Hutchings and others, 2012). The appropriate rheology to describe ice deformation depends on sea ice conditions, such that deformation in central Arctic pack ice given stress from the atmosphere and ocean will be very different from deformation in the MIZ (Herman, 2022). In particular, as the role of internal ice stress decreases, and ice floes are able to move more freely, the time and space scales of sea ice motion are more likely to reflect the scales of atmosphere and ocean forcing (Hutchings and others, 2012).

Numerous methods exist for characterizing ice properties and dynamics in the MIZ, yet gaps in the observation network remain (Gerland and others, 2019; Lee and others, 2022). High resolution images allow a larger portion of the FSD to be resolved (Wang and others, 2016; Stern and others, 2018a), but have limited spatial and temporal availability; differences in spatial resolution and other data limitations make intercomparison challenging (Petty and others, 2021). Standard methods for observing ocean eddies in the world ocean (e.g., Chelton and others (2011)) are unavailable in the Arctic due to gaps in satellite coverage and the presence of sea ice; alternative approaches include manual eddy identification in synthetic aperature radar (SAR) imagery (Kozlov and others, 2019) and using sea surface topography (Kubryakov and others, 2021). Complications with melt onset in summer and subscale grid variability increase the uncertainty of remote sensing measurements of sea ice motion (Meier and others, 2000; Tschudi and others, 2020). Drifting buoy observations provide local estimates with high confidence (Webster and others, 2022), however observations in the Fram Strait and other marginal sea ice regions are sparse (Brunette and others, 2022; Gerland and others, 2019), and low spatial correlation reduces the representiveness of buoy observations.

In this article, we present sea ice observations from the Fram Strait region spanning spring and summer seasons from 2003-2020 derived from daily snapshots from optical satellite imagery using the Ice Floe Tracker algorithm (Lopez-Acosta and others, 2019). These floe-scale, Lagrangian measurements of sea ice motion address a major data gap for sea ice dynamics in the summer marginal ice zone (MIZ). Our focus is on how unique properties of the MIZ contribute to the temporal and spatial scales of sea ice motion, including effects of an evolving floe size distribution (FSD), proximity of the sea ice edge, and the presence of a rich upper ocean eddy field.

The remainder of the paper is as follows. In section 2, we describe the observational data sources and our model setup. In section 3, we describe the analysis methods. Results are presented and discussed in section 4. The paper is concluded in section 5.

DATA

Observations

We obtained Moderate Resolution Imaging Spectroradiometer (MODIS) imagery of the Fram Strait region from the from NASA Earthdata Worldview for April-September of each year from 2003 to 2020. We used mosaic imagery from the ascending passes (approximately local noon) for both the Aqua and Terra satellites. For each mosaic image, we assigned an overpass time using the Satellite Overpass Identification Tool (Hatcher and others, 2022).

We obtain floe-scale sea ice motion from the Ice Floe Tracker (IFT) algorithm. The IFT algorithm is described in Lopez-Acosta and others (2019) and consists of three components: image processing, feature extraction, and floe tracking. The image processing step applies land and cloud masks, increases the contrast between water and ice, and normalizes the image. The processed image is then segmented using k-means clustering and watershed methods. Feature extraction collects shape properties (e.g., area, perimeter, best fit ellipse, centroid) from potential floes. Here we consider only potential floes with at least 300 pixels and at most 90,000 pixels (18.75 km^2 to 5,625 km^2). False positives, including clouds and ice filaments, are removed using a circularity criterion C

$$C = \frac{4\pi A}{P^2}, \tag{2}$$

where A is the floe area and P is the floe perimeter. The maximum circularity value is 1 (a perfect circle). Examining the distribution of C and the library of potential floe shapes from the feature extraction algorithm, we identify a local minimum of 0.6 separating false positives and ice floes. Shapes with $C < 0.6$ are flagged and excluded from the analysis. The total number of floe shapes used in the floe size distribution analysis is marked in orange in Figure 1. On average, 55,000 floes are identified per year; variance year-to-year is related both to the sea ice extent and to varying cloud cover.

The floe tracking component links floe shapes between image pairs. For each floe, candidate matches in subsequent images are first filtered by travel distance and floe area. Potential floe matches are rotated until the area difference is minimized. If the area differences is sufficiently small after rotation, ψ-s curves (Kwok and others, 1990) are calculated for each floe. These curves summarize the tangent angle and perimeter of each floe. If the ψ-s correlation is higher than 0.7, the floes are linked. Whether a floe can be tracked depends on error in the algorithm, varying cloud cover, and on whether the floe remains intact. The green line in Figure 1 shows the number of floe shapes with at least one match. Finally, the purple line in Figure 1 indicates the number of unique floes in the set of floe trajectories. On average, 4,300 unique floes are observed each year.

Daily ascending images from Aqua and Terra are separated in time by between 20 and 90 minutes, typically. Both images are analyzed. Daily rotation rates are calculated separately for the two satellites. We use the mean daily rotation across the two satellites when both are available, otherwise we use rotation from a single satellite. Rotation rates are then normalized to radians per day. Floe positions are regridded to local noon, which is typically less than 2 hours away from the two satellite overpass times. Daily displacements are estimated via forward differences. Displacements are converted into velocity units (m/s).

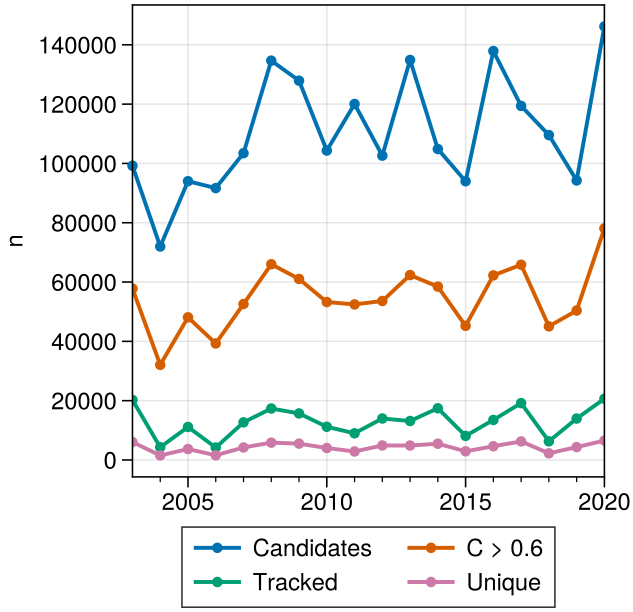

Fig. 1. Sample size of floe observations by year. Blue shows the number of candidate shapes, orange the number of shapes passing the circularity criterion (and thus considered to be ice floes), and green shows the number of tracked floes.

Note that this measure of velocity is not identical with instantaneous velocity, as daily observations only allow measurement of net displacements rather than total path distance traveled per day.

Following the daily displacement velocity estimation we apply an additional set of quality control steps. We flag (a) drift speeds larger than 1.5 m/s (b) floes with maximum drift speed throughout the full trajectory of less than 0.005 m/s (i.e., two pixels per day) and (c) floes with total travel distance of less than 250 m (one pixel) per day.

We use the National Snow and Ice Data Center (NSIDC) Daily Ice Motion Vectors (Tschudi and others, 2020) data product to estimate the time-average sea ice velocity. The ice motion vectors are on a 25 km grid, though the effective resolution is generally coarser. The NSIDC Ice Motion Vectors daily velocity estimates are interpolated linearly to floe positions. We then calculated the centered 5, 15, and 31-day average velocity from the Ice Motion Vectors and interpolate these averages to floe positions.

Sea ice concentration (SIC) data comes from the NSIDC Climate Data Record of Sea Ice Concentration (SIC CDR, Meier and others (2021)). We apply nearest neighbor interpolation to find the sea ice concentration in the nearest grid cell to the IFT floe positions. The distance to the ice edge is approximated by finding the minimum distance between a floe and the set of pixels in the SIC CDR with concentrations between 0 and 30%.

Simulations

We examine the effects of mesoscale and submesoscale oceanic eddies on ice motion using a discrete element sea ice model (SubZero, Manucharyan and Montemuro (2022)) forced by a two-layer quasi-geostrophic (QG) ocean model. We use circular sea ice floes with radii $R_{ice} = 1, 2, \ldots, 29$ km. For each R_{ice}, we randomly place $n = 4,000$ floes onto the QG ocean flow field and allow the floes to be advected by the ocean currents for 30 model days. The main adjustable parameters of the QG model are the bulk vertical shear ΔU, the Rossby deformation radius, R_d, and the top/bottom ocean layer depth ratio δ. Best-fit values of the model $\Delta U = 1.8$ m/s, $R_d = 5.2$ km, and δ=1 were obtained using a loss function based on observed and modeled floe rotation rates with data from the western Arctic Ocean (Beaufort Sea). Ocean model tuning is described in Manucharyan and others (2022). The ocean flow fields were acquired after a simulation year, ensuring statistical equilibration and a constant energy spectrum. Ocean fields were updated daily in the simulation to align the simulation resolution with the temporal resolution of the observed sea ice data. The time step for sea ice floes is set at 0.01 simulation day. 256 Fourier modes were used to simulate domains of 400×400 km in space. While we do not expect the ocean eddy field in the Greenland Sea to be identical to the Beaufort Sea, the model allows us to compare observations to purely eddy-driven sea ice motion.

METHODS

Floe size distribution

A common approach to estimating power law fits from empirical data is to apply a log-transform to the data and fit a line using least squares. However, Clauset and others (2009) point out that this method can be inaccurate due to the effect of sparse but impactful fluctuations in the tail of the distribution, and because the least squares fit is not testing whether the data are following a power law (see also Bauke (2007); Goldstein and others (2004)). By definition, x follows a power law if it's probability distribution $p(x)$ is proportional to $x^{-\beta}$, where β is constant; i.e.

$$p(x)\alpha x^{-\beta} \tag{3}$$

Physical systems typically are bounded, e.g. there exists power law-like behavior between x_{min} and x_{max} so it is more precise to say that a power law describes the tail of the distribution. In statistics a power law is rigorously defined. We follow the approach of Clauset and others (2009), as implemented in the Python `powerlaw` package (Alstott and others, 2014). The method has three main steps. (1) Estimate x_min and β. (2) Calculate goodness of fit - if $p > 0.1$, a power law is a plausible hypothesis for the data. (3) Compare the power law with alternative hypothesis using a likelihood ratio test. ‘

Velocity vector decomposition

The sea ice velocity can be expressed in reference to a mean flow $\overline{u}, \overline{v}$ such that it contains an along-track (longitudinal) component u_L and cross-track (transverse) component u_T, with positive values indicating the direction of mean flow and 90° to the right of the mean flow, respectively. The longitudinal and transverse perturbation velocities u'_L and u'_T can then be computed by subtracting the mean flow from the individual floe velocities, and then calculating the longitudinal and transverse components of the velocity anomalies. Following Gabrielski and others (2015), we use centered-time averages of the NSIDC Ice Motion Vectors product to represent the mean flow. The transverse velocity component is often termed the *perturbation velocity*. Properties of u_T likely depend on the choice of the mean flow (e.g., Rampal and others (2009)), here we consider the effects of different time-average windows $\tau \in (5, 10, 15)$ where τ is time in days.

Strain rate estimation

Area-averaged strain rates can be calculated from sets of point estimates of sea ice velocities by application of Green's theorem (e.g. Kwok and others (2003); Hutchings and others (2012); Rampal and others (2019); Dierking and others (2020)). Given a set of N ice floe positions and velocity estimates x, $u(x)$, we iterate over all possible triangles formed by subsets of floe positions and retain all triangles with minimum interior angle of 20° or greater. This results in 6.6 million polygons; since the number of available polygons is bounded above by a combinatorial function, the number of polygons varies widely per year. We calculate the area of the triangle via

$$A = \frac{1}{2} \sum_{i=1}^{n} \left[x_i y_{i+1} - y_i x_{i+1} \right]. \tag{4}$$

Note that in the summation notation above, the calculation wraps around the polygon to the origin, so for the triangles used here, $x_4 = x_1$. The latitude and longitude coordinates for each floe is projected into Cartesian space via the Lambert Azimuthal Equal Area projection for the area calculation. Interior angles are calculated using the law of cosines. For angle and velocity calculations, we first transform the latitude and longitude coordinates into North Polar Stereographic coordinates. The area-averaged velocity gradients are calculated as

$$\begin{aligned} u_x &= \frac{1}{A}\oint u\,dy \\ &\approx \frac{1}{2A}\sum_{i=1}^{N}\left[(u_{i+1}+u_i)(y_{i+1}-y_i)\right] \end{aligned} \tag{5}$$

and similarly

$$v_x \approx \frac{1}{2A}\sum_{i=1}^{N}\left[(v_{i+1}+v_i)(y_{i+1}-y_i)\right] \tag{6}$$

$$u_y \approx -\frac{1}{2A}\sum_{i=1}^{N}\left[(u_{i+1}+u_i)(x_{i+1}-x_i)\right] \tag{7}$$

$$v_y \approx -\frac{1}{2A}\sum_{i=1}^{N}\left[(v_{i+1}+v_i)(x_{i+1}-x_i)\right]. \tag{8}$$

From these velocity gradients we calculate the strain rate components

$$\dot{\varepsilon}_{shear} = \sqrt{(u_x - v_y)^2 + (u_y + v_x)^2} \tag{9}$$

$$\dot{\varepsilon}_{div} = u_x + v_y \tag{10}$$

$$\dot{\varepsilon}_{vort} = v_x - u_y \tag{11}$$

$$\dot{\varepsilon}_{tot} = \sqrt{\dot{\varepsilon}^2_{shear} + \dot{\varepsilon}^2_{div}}. \tag{12}$$

Uncertainty in the strain rate calculations depends on the uncertainty in position σ_X and area σ_A, and on the velocities. Triangle area uncertainty depends on the side lengths, so for a triangle with sides a, b, c, the uncertainty in area σ_A is given by

$$\sigma_A^2 = \frac{\sigma_X^2}{4}(a^2 + b^2 + c^2) \tag{13}$$

and relative uncertainty in a strain rate component ϵ is given by

$$\frac{\delta_\epsilon}{\epsilon} = 2\left(4\frac{\delta_x^2}{A} + 2\frac{\delta_x^2}{U^2T^2} + \delta_T^2/T^2 + \frac{\delta_A^2}{A^2}\right)^{1/2} \tag{14}$$

From Lopez-Acosta and others (2019), the position error for ice floes is comparable to the resolution of the MODIS imagery, so $\sigma_x \approx 255$ m, and velocity error ≈ 0.65 cm/s. For a right triangle with minimum angle 20, relative area uncertainty is 14% for a 10 km^2 triangle, dropping to 5% for triangles larger than 50 km^2. For the polygons and floe velocities in our data, strain rate relative uncertainties of 10% are typical for individual measurements.

Length scale parameter estimation

Our next task is to estimate the length scale dependence of deformation

$$\dot{\varepsilon}_{tot} \sim L^{-\beta} \tag{15}$$

where L is the length scale of the observation; here, we use $L = \sqrt{A}$. We hypothesize that scaled total deformation

$$\dot{\varepsilon}^*_{tot}(\beta) = \dot{\varepsilon}_{tot}/L^{-\beta} = \dot{\varepsilon}_{tot}L^{\beta} \tag{16}$$

is lognormally distributed. Lognormal distributions arise due to the central limit theorem in the case that independent random variables are combined multiplicatively rather than additively; lognormal distributions are observed in the plastic deformation of numerous materials. Under this assumption, the logarithm of the scaled total deformation is normally distributed

$$\log \dot{\varepsilon}^*_{tot} \sim \mathcal{N}(\mu, \sigma^2) \tag{17}$$

with parameters μ and σ^2 dependent on the parameter β

$$\mu(\beta) = \frac{1}{N}\sum_{i=1}^{N} \log \dot{\varepsilon}^*_{tot,i}(\beta) \tag{18}$$

$$\sigma^2(\beta) = \frac{1}{N}\sum_{i=1}^{N} \left[\log \dot{\varepsilon}^*_{tot,i}(\beta) - \mu(\beta)\right]^2 \tag{19}$$

where N is the total number of triangles. These are, of course, the standard maximum likelihood estimates for the parameters of a normal distribution. However at this stage the β parameter needed to calculate $\dot{\varepsilon}^*_{tot}$ is unknown. Our approach is to numerically find the maximum of the log likelihood function for $\mathcal{N}(\mu, \sigma)$.

The log likelihood function given n observations of deformation $\dot{\varepsilon}_{tot,i}$ and length scale L_i is

$$\begin{aligned}\log \mathcal{L}(\beta|\dot{\varepsilon}_{tot}, L) = &-\frac{n}{2}\log(2\pi\sigma(\beta)^2)\\ &-\frac{1}{\sigma(\beta)^2}\sum_i^n\left[\dot{\varepsilon}_{tot,i} - \mu(\beta))^2\right]\end{aligned} \tag{20}$$

While the ice floe observations from Ice Floe Tracker are a random sample, they are not a uniform random sample in space or time. For example, ice floes cannot be detected when optically thick clouds are present. Furthermore, as the ice melts and evolves through the year, it is likely that the number of floes will change. Hence the number of floes detected will vary over time.

In order to prevent representation bias from affecting our estimates of β we take a stratified sampling approach. We sort the observations into 10 length scale bins ranging in size from 10 km to 300 km. The bin edges are regular in logarithmic space consistent with the parameter being based on the log-transformed data. We consider each month separately and pool all years together. Finally, we take a random sample of 1,000 observations from each length scale bin to form a sample of size 10,000. We emphasize that the bins are used for stratified sampling, and we do not average data within bins prior to estimating the length scale parameter. The parameter β is then estimated numerically by maximizing $\log \mathcal{L}(\beta|\dot{\varepsilon}_{tot}, L)$ over $\beta \in (0, 1]$. We calculate a bootstrap confidence interval for β using the quantile method with 1,000 bootstrap replicates.

RESULTS

Floe size distribution

The power law fit to the floe size distribution reveals a negative slope (α) of 1.44 (Figure 2). The α is on the low range of typical alpha values for previously observed FSDs (Stern and others, 2018b). This could be because the ice exiting the Fram Strait is the thickest and oldest ice in the Arctic, and may be more resilient to break up due to its structural integrity. Uncertainty in floe area depends on the image resolution, and thus small floes have a much higher relative uncertainty. The deviation from the best fit line at floe sizes lower than $\approx$ 100 km^2 may indicate a bias in the retrieval rate of small floes compared to large floes. Nevertheless, the empirical distributions show that sampled floes cover a wide range of sizes. While the lack of small floes needs to be addressed prior to investigating, for example, seasonal or interannual variability in the floe size distribution, the data do allow investigation of the effects of floe size on sea ice

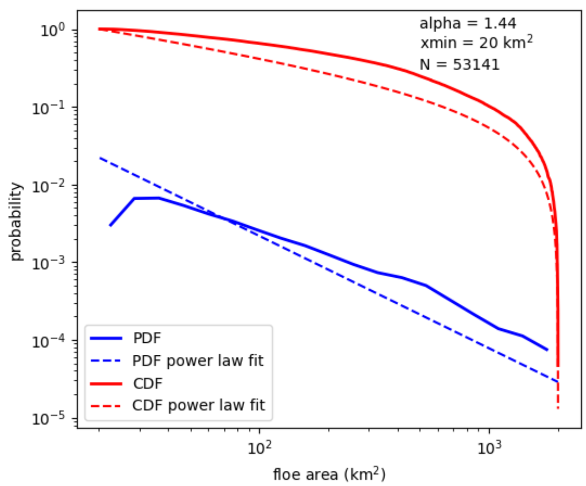

Fig. 2. Floe size distribution for floes identified in the Fram Strait with the Ice Floe Tracker. The probability distribution function (blue) and the complementary cumulative distribution function (red) for the data (solid line) and best fit (dashed line).

motion.

Velocity distribution

The distributions of the scaled velocity perturbations u'_L and u'_T are non-Gaussian (Figure 3). The shape of the distribution is relatively insensitive to the choice of averaging timescale tau used for computing the background flow field. Differences in standard deviations between the three τ values are O(0.1) cm/s, ranging from 8.8-9.1 cm/s for the longitudinal component and from 6.5-6.9 cm/s for the transverse component. As the fluctuating velocity distributions show little tau dependence, we focus on results for $\tau = 5D$ hereafter.

We now consider the role of ocean eddies, floe size, and distance to the ice edge on the velocity anomaly distributions. Non-Gaussian velocity anomaly distributions have been observed in sea ice in the central Arctic have been noted by Rampal and others (2009), and for open ocean drifters by Bracco and others (2000). The physical reasons for non-Gaussian velocity distributions may differ in the MIZ compared to the central Arctic. The QG model simulations test whether an ocean eddy field could produce the observed velocity characteristics. We find that the simulated velocity distributions show excellent agreement with the observations (Figure 4a-b). From this, we see that in the absence of winds, a turbulent ocean alone can produce sea ice velocity anomalies with the observed non-Gaussian distribution. Considering the standard

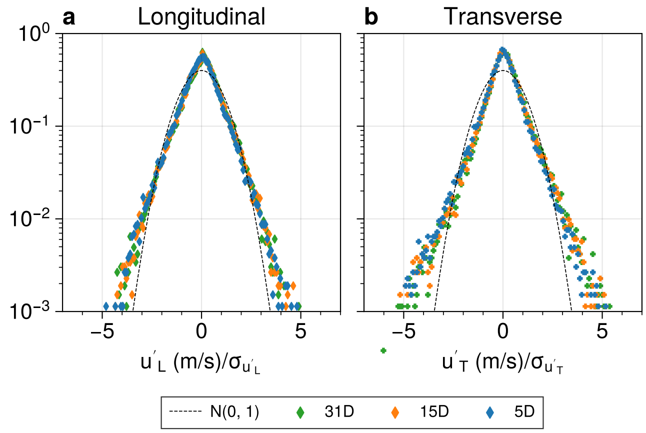

Fig. 3. Empirical probability distribution functions (PDFs) of scaled longitudinal (a) and transverse (b) velocity perturbations of Ice Floe Tracker floe displacements with respect to the 5-day (blue circles), 15-day (orange crosses), and 31-day (green squares) centered mean NSIDC gridded ice motion. Black lines show the PDF of a normal distribution with mean 0 and standard deviation 1.

deviations $\sigma_{u'}$ of observations (within 2 km length bins) against the simulation results, we find in both cases that $\sigma_{u'}$ decreases as the floe size increases (Figure 4c). However, the observed $\sigma_{u'}$ is much larger than in the simulations. While there is a difference between longitudinal and transverse components in the simulations, with simulated transverse $\sigma_{u'}$ slightly larger, we find the observed longitudinal $\sigma_{u'}$ to be notably larger than transverse $\sigma_{u'}$.

The Beaufort Sea is known to have a less energetic eddy field than the Greenland Sea (Armitage and others (2017), e.g.). A QG-model tuned to the Greenland Sea would likely have different properties than the model we used. Secondly, the simulations are showing the velocity distribution in the absence of floe interactions, large-scale currents, and wind forcing. It is likely the case that the presence of a rapidly varying wind field would amplify the sea ice velocity perturbations. Model results presented by Rallabandi and others (2023) suggest that a stochastic wind field and interacting sea ice floes can also produce non-Gaussian sea ice velocity distributions. In any case, the results underscore the need for eddy-resolving ocean currents to correctly simulate ice motion in the MIZ.

The QG model simulates a homogeneous ocean. The position of the ice edge, coast interactions, and highly variable, shallow bathymetry produce a heterogeneous seascape in the Greenland Sea. From Figure 4d, we see a strong dependence of $\sigma_{u'}$ on the proximity of the sea ice edge. The proximity of the ice edge reduces internal ice stress. More important, however, may be the effects of coupled air-ice-ocean interactions.

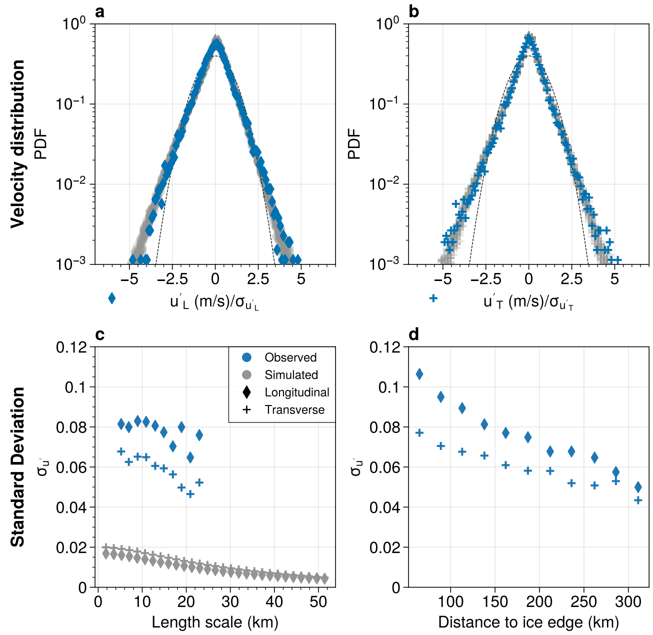

Fig. 4. Observed (blue) and simulated (gray) scaled velocity distributions (top) and standard deviations (bottom). As in Figure 3, a reference $N(0,1)$ distribution is shown in panels a and b with a dotted line. Observed $\sigma_{u'}$ in (c) and (d) are bin averages. In (c), 2 km bins are used, while in (d), 25 km bins are used. Only bins with at least 300 observations are shown. Length scale is the square root of floe area.

The FSD affects the velocity field by determining the scales of local velocity correlations. While the dependence is not as strong as with the distance to ice edge, we find higher standard deviations of the fluctuating velocities for small floes relative to large floes (Figure 4b), indicating larger departures from the local mean flow field.

Rotation rates

The ability of Ice Floe Tracker to resolve sea ice rotation is a key advancement for remote sensing of sea ice motion. However, in the current version of the algorithm, the number of measured rotation rates is much smaller than the number of resolved floes, as a rotation rate can only be calculated for tracked floes where the floe is observed by the same satellite on two consecutive days. Nevertheless, enough rotation rates were calculated to examine the relationship between floe size and rotation rates.

In both the simulations and the observations, we see a narrowing of the rotation rate distribution as floe size increases (Figure 5). The highest rotation rates are seen in the smallest floes. Since a sea ice floe moves as a solid body, ocean stresses are integrated across the full floe. The lower rotation rates of

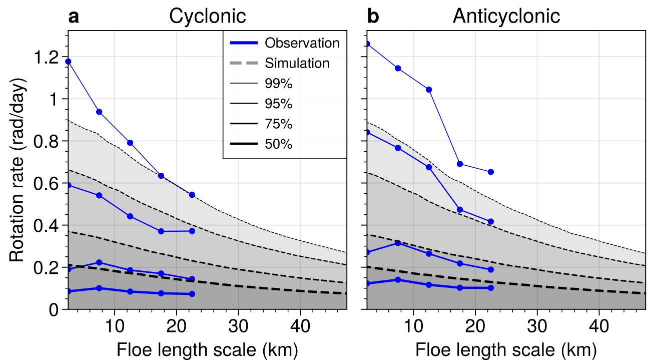

Fig. 5. Observed (blue lines) and simulated (gray shading, black dashed lines) rotation rate percentiles versus floe length scale. Observation percentiles are calculated within 5 km length scale bins. Only bins with at least 100 observations are shown. Lines from thickest to thinnest indicates the 50th, 75th, 95th, and 99th percentiles.

large floes may then reflects the ocean currents varying over smaller scales than the size of the floe. The relationship between ocean vorticity and floe shape depends on the size scales of ocean eddies and sea ice floes. The detailed kinematics of the eddy-floe size relationship will be addressed in a future publication.

The observed rotation rate distributions, while showing a similar scale dependence as the simulations, have narrower peaks and wider tails. The floe observations are not limited to low sea ice concentrations. The narrow peak may therefore indicate constraints on the rotation rate from floe interactions, while the wider tails may arise from the more energetic eddy field in the Greenland Sea compared to the simulations.

Deformation length scales

Total deformation decreases with increasing length scale (Figure 6). Estimated length scale parameters range from $\beta = 0.59$ in April to $\beta = 0.65$ in May; based on the bootstrap confidence intervals, the May parameter is highest, however the practical difference is not large. These scaling parameters are much steeper than has been observed in the central Arctic winter pack ice (e.g., $\beta = 0.21$ in Hutchings and others (2012) and $\beta = 0.2$ in Marsan and others (2004)), and is similar to the values found for small length scales by Oikkonen and others (2017). They found β increasing from 0.52 to 0.82 as the time interval decreased from 24 hours to 10 minutes. They further found lower deformation rates as the distance from the ice edge increased.

Comparison of the log-transformed scaled deformation rates with a normal distribution in a probability plot (not shown) indicates that the deformation rates are left-skewed, i.e., small deformation rates are more frequent than would be expected given the μ and σ^2 parameters given in equations 18 and 19. Given the

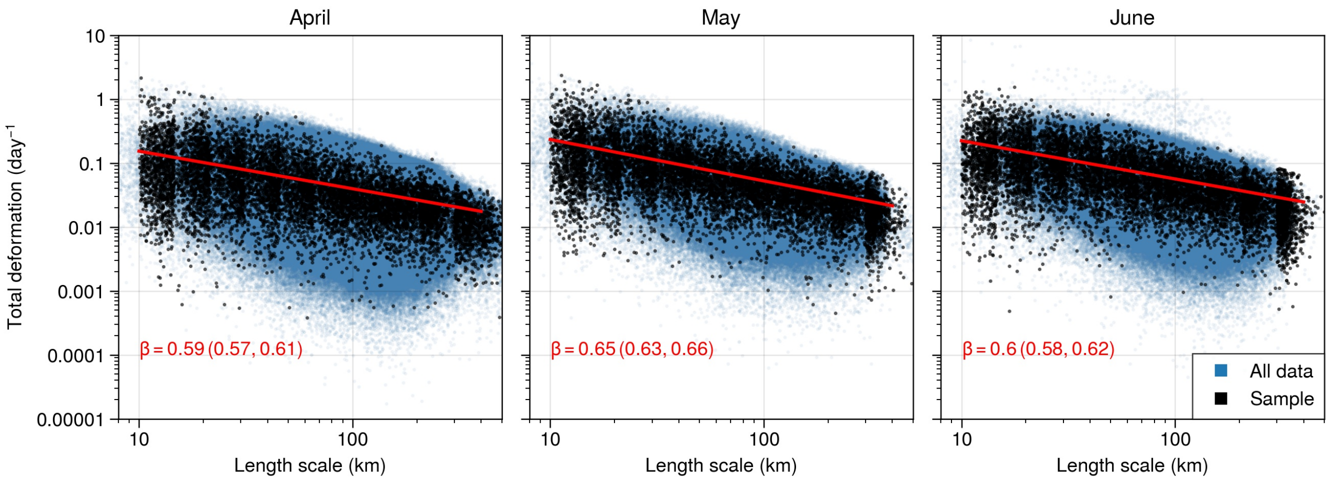

Fig. 6. Total deformation as a function of length scale for all polygons (blue) and for the stratified sample (black) for (a) May, (b) June, and (c) July. The maximum likelihood estimate for β assuming a lognormal distribution is shown with the red line. The length scale parameter β and corresponding bootstrap 95% confidence intervals are provided in the lower left of each panel.

known strong gradients in the East Greenland Sea ice velocity field it is likely that the skewed distributions are a result of including regions with different deformation properties. We can expect stronger deformation where sea ice concentration is lower, and we can expect there to be stronger deformation near the sea ice edge.

CONCLUSIONS

The floe-scale observations presented here represent a new category of observations for the summer marginal ice zone. These observations complement existing in situ and remote sensing techniques by increasing the sample size of floe-scale displacement observations in the MIZ relative to available drifting buoy observations, by linking floe shapes with ice dynamics, and by producing floe rotation rates. The observations provide point estimates of ice displacements in a season and location where other observations are lacking or have high uncertainty: during the melt season and in the marginal ice zone.

We showed observational and model-based evidence that the both sea ice velocity anomalies and rotation rates are related to the floe size. In particular, as floe size increases, the scale of the velocity anomaly and rotation rate distributions decreases. The simulations show that the observed scale dependence can arise from ocean turbulence in the absence of winds and large-scale currents. This study marks the first time, to our knowledge, that the deformation length scales parameter in the MIZ has been calculated using floe-scale remote sensing observations. Further work will examine the interannual variability in the deformation length scale.

A major motivation of the work presented here is to enable model development, including new parameterizations of FSD effects in sea ice models and representation of mesoscale and submesoscale sea ice-ocean interactions. Work toward improved metrics for discrete element sea ice models is underway.

ACKNOWLEDGEMENTS

DW and MMW were supported by NASA The Science of Terra, Aqua, and Suomi-NPP Program (20-TASNPP20-0202). EB and MMW were supported by Office of Naval Research (ONR) Arctic Program (N00014-20-1-2753, N00014-22-1-2741, and N00014-22-1-2722) and the ONR Multidisciplinary University Research Initiatives Program (N00014-23-1-2014). MK was supported by ONR grant N00014-22-1-2741.

We acknowledge the use of MODIS True Color Corrected Reflectance imagery from the Terra and Aqua satellites aquired via the from the Worldview Snapshots application (https://wvs.earthdata.nasa.gov), part of the Earth Observing System Data and Information System (EOSDIS).

REFERENCES

Alstott J, Bullmore E and Plenz D (2014) Powerlaw: A Python Package for Analysis of Heavy-Tailed Distributions. *PLoS ONE*, **9**(1), e85777, ISSN 1932-6203 (doi: 10.1371/journal.pone.0085777)

Armitage TWK, Bacon S, Ridout AL, Petty AA, Wolbach S and Tsamados M (2017) Arctic Ocean surface geostrophic circulation 2003–2014. *The Cryosphere*, **11**(4), 1767–1780, ISSN 1994-0424 (doi: 10.5194/tc-11-1767-2017)

Bauke H (2007) Parameter estimation for power-law distributions by maximum likelihood methods. *The European Physical Journal B*, **58**(2), 167–173, ISSN 1434-6028, 1434-6036 (doi: 10.1140/epjb/e2007-00219-y)

Bracco A, LaCasce JH and Provenzale A (2000) Velocity Probability Density Functions for Oceanic Floats. *Journal of Physical Oceanography*, **30**(3), 461–474, ISSN 0022-3670, 1520-0485 (doi: 10.1175/1520-0485(2000)030<0461:VPDFFO>2.0.CO;2)

Brunette C, Tremblay LB and Newton R (2022) A new state-dependent parameterization for the free drift of sea ice. *Cryosphere*, **16**(2), 533–557, ISSN 19940424 (doi: 10.5194/tc-16-533-2022)

Chelton DB, Schlax MG and Samelson RM (2011) Global observations of nonlinear mesoscale eddies. *Progress in Oceanography*, **91**(2), 167–216, ISSN 00796611 (doi: 10.1016/j.pocean.2011.01.002)

Clauset A, Shalizi CR and Newman MEJ (2009) Power-Law Distributions in Empirical Data. *SIAM Review*, **51**(4), 661–703, ISSN 0036-1445, 1095-7200 (doi: 10.1137/070710111)

Dai HJ, McWilliams JC and Liang JH (2019) Wave-driven mesoscale currents in a marginal ice zone. *Ocean Modelling*, **134**, 1–17, ISSN 14635003 (doi: 10.1016/j.ocemod.2018.11.006)

Dierking W, Stern HL and Hutchings JK (2020) Estimating statistical errors in retrievals of ice velocity and deformation parameters from satellite images and buoy arrays. *The Cryosphere*, **14**, 2999–3016 (doi: 10.5194/tc-14-2999-2020)

Dumont D (2022) Marginal ice zone dynamics: History, definitions and research perspectives. *Philosophical Transactions of the Royal Society A: Mathematical, Physical and Engineering Sciences*, **380**(2235), 20210253, ISSN 1364-503X, 1471-2962 (doi: 10.1098/rsta.2021.0253)

Gabrielski A, Badin G and Kaleschke L (2015) Anomalous dispersion of sea ice in the Fram Strait region. *Journal of Geophysical Research: Oceans*, **120**(3), 1809–1824 (doi: 10.1002/2014JC010359)

Geise GR, Barton CC and Tebbens SF (2017) Power Scaling and Seasonal Changes of Floe Areas in the Arctic East Siberian Sea. *Pure and Applied Geophysics*, **174**(1), 387–396, ISSN 0033-4553, 1420-9136 (doi: 10.1007/s00024-016-1364-2)

Gerland S, Barber D, Meier W, Mundy CJ, Holland M, Kern S, Li Z, Michel C, Perovich DK and Tamura T (2019) Essential gaps and uncertainties in the understanding of the roles and functions of Arctic sea ice. *Environmental Research Letters*, **14**(4), 043002, ISSN 1748-9326 (doi: 10.1088/1748-9326/ab09b3)

Goldstein ML, Morris SA and Yen GG (2004) Problems with fitting to the power-law distribution. *The European Physical Journal B*, **41**(2), 255–258, ISSN 1434-6028, 1434-6036 (doi: 10.1140/epjb/e2004-00316-5)

Guest P, Persson POG, Wang S, Jordan M, Jin Y, Blomquist B and Fairall C (2018) Low-Level Baroclinic Jets Over the New Arctic Ocean. *Journal of Geophysical Research: Oceans*, **123**(6), 4074–4091, ISSN 21699291 (doi: 10.1002/2018JC013778)

Hakkinen S (1987) Feedback between ice flow, barotropic flow, and baroclinic flow in the presence of bottom topography. *Journal of Geophysical Research: Oceans*, **92**(C4), 3807–3820 (doi: 10.1029/JC092iC04p03807)

Hatcher S, Ahmed A, Kim M and Wilhelmus MM (2022) SOIT: Satellite overpass identification tool. Zenodo (doi: 10.5281/zenodo.6475619)

Heorton HDBS, Feltham DL and Hunt JCR (2014) The Response of the Sea Ice Edge to Atmospheric and Oceanic Jet Formation. *Journal of Physical Oceanography*, **44**(9), 2292–2316, ISSN 0022-3670, 1520-0485 (doi: 10.1175/JPO-D-13-0184.1)

Herman A (2022) Granular effects in sea ice rheology in the marginal ice zone. *Philosophical Transactions of the Royal Society A: Mathematical, Physical and Engineering Sciences*, **380**(2235), 20210260, ISSN 1364-503X, 1471-2962 (doi: 10.1098/rsta.2021.0260)

Hibler WD (1979) A Dynamic Thermodynamic Sea Ice Model. *Journal of Physical Oceanography*, **9**(4), 815–846, ISSN 0022-3670 (doi: 10.1175/1520-0485(1979)009<0815:ADTSIM>2.0.CO;2)

Hutchings JK, Heil P, Steer A and Hibler WD (2012) Subsynoptic scale spatial variability of sea ice deformation in the western Weddell Sea during early summer. *Journal of Geophysical Research*, **117**(C1), C01002, ISSN 0148-0227 (doi: 10.1029/2011JC006961)

Hutter N, Losch M and Menemenlis D (2018) Scaling Properties of Arctic Sea Ice Deformation in a High-Resolution Viscous-Plastic Sea Ice Model and in Satellite Observations. *Journal of Geophysical Research: Oceans*, **123**(1), 672–687, ISSN 2169-9275, 2169-9291 (doi: 10.1002/2017JC013119)

Hwang B, Wilkinson J, Maksym T, Graber HC, Schweiger A, Horvat C, Perovich DK, Arntsen AE, Stanton TP, Ren J and Wadhams P (2017) Winter-to-summer transition of Arctic sea ice breakup and floe size distribution in the Beaufort Sea. *Elementa: Science of the Anthropocene*, **5**, 40, ISSN 2325-1026 (doi: 10.1525/elementa.232)

Inoue J (2004) Ice floe distribution in the Sea of Okhotsk in the period when sea-ice extent is advancing. *Geophysical Research Letters*, **31**(20), L20303, ISSN 0094-8276 (doi: 10.1029/2004GL020809)

Johannessen JA, Johannessen OM, Svendsen E, Shuchman R, Manley T, Campbell WJ, Josberger EG, Sandven S, Gascard JC, Olaussen T, Davidson K and Van Leer J (1987) Mesoscale eddies in the Fram Strait marginal ice zone during the 1983 and 1984 Marginal Ice Zone Experiments. *Journal of Geophysical Research*, **92**(C7), 6754, ISSN 0148-0227 (doi: 10.1029/JC092iC07p06754)

Kozlov IE and Atadzhanova OA (2021) Eddies in the Marginal Ice Zone of Fram Strait and Svalbard from Spaceborne SAR Observations in Winter. *Remote Sensing*, **14**(1), 134, ISSN 2072-4292 (doi: 10.3390/rs14010134)

Kozlov IE, Artamonova AV, Manucharyan GE and Kubryakov AA (2019) Eddies in the Western Arctic Ocean From Spaceborne SAR Observations Over Open Ocean and Marginal Ice Zones. *Journal of Geophysical Research: Oceans*, **124**(9), 6601–6616, ISSN 2169-9275, 2169-9291 (doi: 10.1029/2019JC015113)

Kubryakov AA, Kozlov IE and Manucharyan GE (2021) Large Mesoscale Eddies in the Western Arctic Ocean From Satellite Altimetry Measurements. *Journal of Geophysical Research: Oceans*, **126**(5), e2020JC016670, ISSN 2169-9275, 2169-9291 (doi: 10.1029/2020JC016670)

Kwok R (2006) Contrasts in sea ice deformation and production in the Arctic seasonal and perennial ice zones. *Journal of Geophysical Research*, **111**(C11), C11S22, ISSN 0148-0227 (doi: 10.1029/2005JC003246)

Kwok R, Curlander J, McConnell R and Pang S (1990) An ice-motion tracking system at the Alaska SAR facility. *IEEE Journal of Oceanic Engineering*, **15**(1), 44–54, ISSN 03649059 (doi: 10.1109/48.46835)

Kwok R, Cunningham GF and Hibler WD (2003) Sub-daily sea ice motion and deformation from RADARSAT observations: SHORT PERIOD ICE MOTION. *Geophysical Research Letters*, **30**(23), n/a–n/a, ISSN 00948276 (doi: 10.1029/2003GL018723)

Lee C, DeGrandpre M, Guthrie J, Hill V, Kwok R, Morison J, Cox C, Singh H, Stanton T and Wilkinson J (2022) Emerging Technologies and Approaches for In Situ, Autonomous Observing in the Arctic. *Oceanography*, ISSN 10428275 (doi: 10.5670/oceanog.2022.127)

Lopez-Acosta R, Schodlok MP and Wilhelmus MM (2019) Ice Floe Tracker: An algorithm to automatically retrieve Lagrangian trajectories via feature matching from moderate-resolution visual imagery. *Remote Sensing of Environment*, **234**(October), 111406, ISSN 00344257 (doi: 10.1016/j.rse.2019.111406)

Manley TO (1987) Effects of sub-ice mesoscale features within the marginal ice zone of Fram Strait. *Journal of Geophysical Research: Oceans*, **92**(C4), 3944–3960, ISSN 0148-0227 (doi: 10.1029/JC092iC04p03944)

Manucharyan GE and Montemuro BP (2022) SubZero: A Sea Ice Model With an Explicit Representation of the Floe Life Cycle. *Journal of Advances in Modeling Earth Systems*, **14**(12), e2022MS003247, ISSN 1942-2466, 1942-2466 (doi: 10.1029/2022MS003247)

Manucharyan GE, Lopez-Acosta R and Wilhelmus MM (2022) Spinning ice floes reveal intensification of mesoscale eddies in the western Arctic Ocean. *Scientific Reports*, **12**(1), 7070, ISSN 2045-2322 (doi: 10.1038/s41598-022-10712-z)

Marsan D, Stern H, Lindsay R and Weiss J (2004) Scale dependence and localization of the deformation of arctic sea ice. *Physical Review Letters*, **93**(17), 3–6, ISSN 00319007 (doi: 10.1103/PhysRevLett.93.178501)

Martin S and Thorndike AS (1985) Dispersion of sea ice in the Bering Sea. *Journal of Geophysical Research*, **90**(C4), 7223–7226, ISSN 01480227 (doi: 10.1029/JC090iC04p07223)

McNutt SL and Overland JE (2003) Spatial hierarchy in Arctic sea ice dynamics. *Tellus A: Dynamic Meteorology and Oceanography*, **55**(2), 181–191 (doi: 10.3402/tellusa.v55i2.12088)

Meier WN, Maslanik JA and Fowler CW (2000) Error analysis and assimilation of remotely sensed ice motion within an Arctic sea ice model. *Journal of Geophysical Research: Oceans*, **105**(C2), 3339–3356, ISSN 01480227 (doi: 10.1029/1999JC900268)

Meier WN, Fetterer F, Windnagel AK and Stewart S (2021) NOAA / NSIDC Climate Data Record of Passive Microwave Sea Ice Concentration, Version 4

Oikkonen A, Haapala J, Lensu M, Karvonen J and Itkin P (2017) Small-scale sea ice deformation during N-ICE2015: From compact pack ice to marginal ice zone. *Journal of Geophysical Research*, **122**, 5105–5120

Perovich DK and Jones KF (2014) The seasonal evolution of sea ice floe size distribution. *Journal of Geophysical Research: Oceans*, **119**(12), 8767–8777, ISSN 21699275 (doi: 10.1002/2014JC010136)

Petty AA, Bagnardi M, Kurtz NT, Tilling R, Fons S, Armitage T, Horvat C and Kwok R (2021) Assessment of ICESat-2 Sea Ice Surface Classification with Sentinel-2 Imagery: Implications for Freeboard and New Estimates of Lead and Floe Geometry. *Earth and Space Science*, **8**(3), e2020EA001491, ISSN 2333-5084, 2333-5084 (doi: 10.1029/2020EA001491)

Rallabandi B, Shaddy B and Greaney AP (2023) Transport of sea ice driven by fluctuating winds

Rampal P, Weiss J, Marsan D, Lindsay R and Stern H (2008) Scaling properties of sea ice deformation from buoy dispersion analysis. *Journal of Geophysical Research: Oceans*, **113**(3), 1–12, ISSN 21699291 (doi: 10.1029/2007JC004143)

Rampal P, Weiss J and Marsan D (2009) Positive trend in the mean speed and deformation rate of Arctic sea ice, 1979-2007. *Journal of Geophysical Research: Oceans*, **114**(5), 1–14, ISSN 21699291 (doi: 10.1029/2008JC005066)

Rampal P, Dansereau V, Olason E, Bouillon S, Williams T, Korosov A and Samaké A (2019) On the multi-fractal scaling properties of sea ice deformation. *The Cryosphere*, **13**(9), 2457–2474, ISSN 1994-0424 (doi: 10.5194/tc-13-2457-2019)

Rothrock DA and Thorndike AS (1984) Measuring the sea ice floe size distribution. *Journal of Geophysical Research*, **89**(C4), 6477, ISSN 0148-0227 (doi: 10.1029/JC089iC04p06477)

Stern HL and Lindsay RW (2009) Spatial scaling of Arctic sea ice deformation. *Journal of Geophysical Research: Oceans*, **114**(10), 1–10, ISSN 21699291 (doi: 10.1029/2009JC005380)

Stern HL, Schweiger AJ, Stark M, Zhang J, Steele M and Hwang B (2018a) Seasonal evolution of the sea-ice floe size distribution in the Beaufort and Chukchi seas. *Elementa: Science of the Anthropocene*, **6**, 48, ISSN 2325-1026 (doi: 10.1525/elementa.305)

Stern HL, Schweiger AJ, Zhang J and Steele M (2018b) On reconciling disparate studies of the sea-ice floe size distribution. *Elementa: Science of the Anthropocene*, **6**, 49, ISSN 2325-1026 (doi: 10.1525/elementa.304)

Sumata H, Lavergne T, Girard-Ardhuin F, Kimura N, Tschudi MA, Kauker F, Karcher M and Gerdes R (2014) An intercomparison of Arctic ice drift products to deduce uncertainty estimates. *Journal of Geophysical Research: Oceans*, **119**(8), 4887–4921, ISSN 21699275 (doi: 10.1002/2013JC009724)

Thorndike AS (1986) Diffusion of sea ice. *Journal of Geophysical Research*, **91**(C6), 7691, ISSN 0148-0227 (doi: 10.1029/JC091iC06p07691)

Timmermans ML, Toole J, Proshutinsky A, Krishfield R and Plueddemann A (2008) Eddies in the Canada Basin, Arctic Ocean, Observed from Ice-Tethered Profilers. *Journal of Physical Oceanography*, **38**(1), 133–145, ISSN 1520-0485, 0022-3670 (doi: 10.1175/2007JPO3782.1)

Tschudi MA, Meier WN and Stewart JS (2020) An enhancement to sea ice motion and age products at the National Snow and Ice Data Center (NSIDC). *The Cryosphere*, **14**(5), 1519–1536, ISSN 1994-0424 (doi: 10.5194/tc-14-1519-2020)

Von Appen WJ, Baumann T, Janout M, Koldunov N, Lenn YD, Pickart R, Scott R and Wang Q (2022) Eddies and the Distribution of Eddy Kinetic Energy in the Arctic Ocean. *Oceanography*, ISSN 10428275 (doi: 10.5670/oceanog.2022.122)

Wang Y, Holt B, Erick Rogers W, Thomson J and Shen HH (2016) Wind and wave influences on sea ice floe size and leads in the Beaufort and Chukchi Seas during the summer-fall transition 2014. *Journal of Geophysical Research: Oceans*, **121**(2), 1502–1525, ISSN 2169-9275, 2169-9291 (doi: 10.1002/2015JC011349)

Watkins DM, Bliss AC, Hutchings JK and Wilhelmus MM (2023) Evidence of Abrupt Transitions Between Sea Ice Dynamical Regimes in the East Greenland Marginal Ice Zone. *Geophysical Research Letters*, **50**(e2023GL103558), 1–10

Webster M, Rigor I and Wright N (2022) Observing Arctic Sea Ice. *Oceanography*, ISSN 10428275 (doi: 10.5670/oceanog.2022.115)

Zhang J (2021) Sea Ice Properties in High-Resolution Sea Ice Models. *Journal of Geophysical Research: Oceans*, **126**(1), ISSN 2169-9275, 2169-9291 (doi: 10.1029/2020JC016686)

Zhang Y, Maslowski W and Semtner AJ (1999) Impact of mesoscale ocean currents on sea ice in high-resolution Arctic ice and ocean simulations. *Journal of Geophysical Research: Oceans*, **104**(C8), 18409–18429, ISSN 21699291 (doi: 10.1029/1999jc900158)